COMMUNICATION

Influence of transition metal electronegativity on the oxygen storage capacity of perovskite oxides†

Lu Liu,[a] Daniel D. Taylor,[b] Efrain E. Rodriguez[a] and Michael R. Zachariah*[ac]

The selection of highly efficient oxygen carriers (OCs) is a key step necessary for the practical development of chemical looping combustion (CLC). In this study, a series of ABO_3 perovskites, where A = La, Ba, Sr, Ca and B = Cr, Mn, Fe, Co, Ni, Cu, are synthesized and tested in a fixed bed reactor for reactivity and stability as OCs with CH_4 as the fuel. We find that the electronegativity of the transition metal on the B-site (λ_B), is a convenient descriptor for oxygen storage capacity (OSC) of our perovskite samples. By plotting OSC for total methane oxidation against λ_B, we observe an inverted volcano plot relationship. These results could provide useful guidelines for perovskite OC design and their other energy related applications.

Chemical looping combustion (CLC) is a novel approach towards the combustion of fuels that utilizes a two-step redox process to achieve carbonaceous combustion, offering a smaller carbon footprint with no thermodynamic energy penalty.[1,2] Instead of directly burning hydrocarbon in air, metal oxides are used as oxygen carriers (OC's) in the fuel reactor where they are reduced while carbonaceous fuel is converted to carbon dioxide and water. The reduced OC's are regenerated in an air reactor, and through cycling these oxides, a flameless combustion is achieved with the temperature in air reactors often lower than 1000 °C, thus avoiding NO_x formation that is generated from traditional combustion with air ($\sim 80\% \ N_2$).[3] The resultant process under ideal conditions generates a pure CO_2 stream, after steam condensation in the fuel reactor.

One of the significant roadblocks in implementation of CLC is finding the right OC, and the multiple considerations include high phase stability, redox activity, low cost, and being environmentally benign.[4] Potential candidates studied as OC's include binary oxides of first row transition metals, such as iron, copper, nickel, manganese, cobalt, and their mixed metal oxides.

Perovskites have also been explored as novel OC's considering their high redox cyclic stabilities and superior oxygen transport capacities.[5] Perovskites are generally formularized as ABO_3, with A and B cations and the O^{2-} anion and are natural candidates for OC's due to their high oxygen conductivity, thermal stability, ease of synthesis, and relatively low cost. In the perovskite structure, the A cation is typically an alkali, alkaline earth, or lanthanide metal, and the B cation a transition metal. Nevertheless, given the myriad of potential combinations of the A and B cations, choosing the optimal perovskite for CLC applications is daunting.[6]

The role of the transition metal B is more important than that of A considering that it is the redox active metal that participates in the CLC reactions. Therefore, we have conducted a systematic study of 9 different $La_{1-x}Ca_xBO_3$ compositions where the B site was varied between Cr to Cu. Furthermore, we included $Ba_{0.5}Sr_{0.5}Co_{0.8}Fe_{0.2}O_3$ (BSCF) since it is a commonly used material in oxygen evolution catalysis. In this communication we report trends of particular materials descriptors such as electronegativity *versus* our independent variable oxygen storage capacity (OSC) with CH_4 as the fuel. Our goal is to find various descriptors that could be utilized by future studies to select the optimal oxides for various CLC applications.

All samples were prepared using an aerosol-assisted spray pyrolysis method as explained in more detail in Section S1 of the ESI.† Briefly, precursor nitrates were dissolved in water, atomized, then decomposed into the resultant perovskite metal oxides in a furnace. This technique ensures homogeneous mixing of elements; and large surface area and low crystallinity of resulting powders. Nanometer scale particles with a spherical morphology were formed for all samples. Representative SEM images of $LaCrO_3$ are shown in Fig. S1 of the ESI.†

Powder X-ray Diffraction (XRD) experiments, performed on a Bruker D8 diffractometer with Cu Kα radiation, were used to characterize the as-synthesized materials – shown in Fig. S2 of the ESI.† Table S1, provided in the ESI,† presents the refined space group, crystallite size, and lattice parameters resulting from Le Bail fitting for each pattern. All refinements were performed with the TOPAS 4.2 software.[7] While most samples

[a] *Department of Chemistry and Biochemistry, University of Maryland, College Park, MD 20742, USA. E-mail: mrz@umd.edu*

[b] *Department of Materials Science and Engineering, University of Maryland, College Park, MD 20742, USA*

[c] *Department of Chemical and Biomolecular Engineering, University of Maryland, College Park, MD 20742, USA*

could be adequately fit in the cubic space group and therefore should be considered pseudocubic, final refinements were performed in either cubic ($Pm\bar{3}m$), orthorhombic ($Pbnm$), or rhombohedral ($R\bar{3}c$) space groups depending on the presence of peak splitting and satellite peaks. Each sample had a crystallite size smaller than 35 nm, determined by the Scherrer equation, as expected with this synthesis technique. The exceptions being $LaMn_{0.5}Ni_{0.5}O_3$ and $Ba_{0.5}Sr_{0.5}Co_{0.8}Fe_{0.2}O_3$ which had crystallite sizes of 77.8(5) and 66.3(4) nm, respectively. Each sample was phase pure except for $LaMn_{0.5}Cu_{0.5}O_3$, $LaCoO_3$, and $La_{0.5}Ca_{0.5}CoO_3$. $LaCoO_3$ and $La_{0.5}Ca_{0.5}CoO_3$ both had a weak and broad peak at approximately $28.5°$ 2θ (approximately 3.0 Å). This peak could be attributed to La_2O_3, however, it is not possible to definitively identify this phase as there are no other impurity peaks present at higher angles in the XRD patterns. For $LaMn_{0.5}Cu_{0.5}O_3$ there are impurity peaks present at approximately 29.5 and $35.5°$ 2θ (approximately 3.0 and 2.5 Å, respectively). The peak at $29.5°$ 2θ can possibly be attributed to La_2O_3 or Cu_2O and the peak at $35.5°$ 2θ to CuO. As with the previous samples, the lack of additional impurity peaks makes the definitive identification of these phases impossible. Other phases considered but ruled out include calcium oxide and carbonate, binary metal oxides, the metallic elements, and all oxygen deficient perovskite based phases present in the ICDD PDF-2 database.

Powder XRD patterns were also collected on the post CLC reactor study samples. Each of these patterns is provided in Fig. S4 of the ESI.† Le Bail fitting of each pattern showed that each sample was phase pure with all peaks being indexed in either the cubic ($Pm\bar{3}m$), orthorhombic ($Pbnm$), or rhombohedral ($R\bar{3}c$) space groups. Representative Le Bail refinements for $La_{0.5}Ca_{0.5}CoO_3$, $LaCu_{0.5}Mn_{0.5}O_3$, and $LaNiO_3$ are provided in Fig. S5–S7 of the ESI.† Table S2, provided in the ESI,† presents the refined space group, crystallite size, and lattice parameters resulting from the Le Bail fitting of each pattern. Considering impurity phases are no longer present in the post fixed bed experiment samples and that the OSC of these samples is steady over the 50 cycles tested, these impurity phases appear to have a minimal effect on the performance of these samples as oxygen carriers.

All but two samples, $LaMn_{0.5}Ni_{0.5}O_3$ and $Ba_{0.5}Sr_{0.5}Co_{0.8}Fe_{0.2}O_3$, experienced an increase in crystallite size, as determined by the Scherrer equation. This suggests that the powders are sintering as they are held at 750 °C during the fixed bed experiments. This sintering can be seen as the diffraction peaks sharpening and the appearance of clear satellite peaks. Further evidence for this sintering is provided by TEM and SEM experiments shown in Fig. S3 of the ESI.† Here, (a) TEM, (b) HRTEM, and (c) SEM images, along with a (d) selected area electron diffraction (SAED) image are provided for $La_{0.5}Ca_{0.5}CoO_3$. The particle morphology became less spherical and agglomerates are beginning to form. Interestingly, this sintering does not appear to affect the OSC for each sample as the delta value remains fairly consistent across 50 cycles (Fig. 1a) consistent with the observations of others.[8,9]

TGA-MS data in Fig. S8, of the ESI,† implies that our perovskites did not spontaneously release O_2 up to 750 °C under an Argon flow, thus suggesting the reaction between the OC and CH_4 follows a gas-solid reaction mechanism.
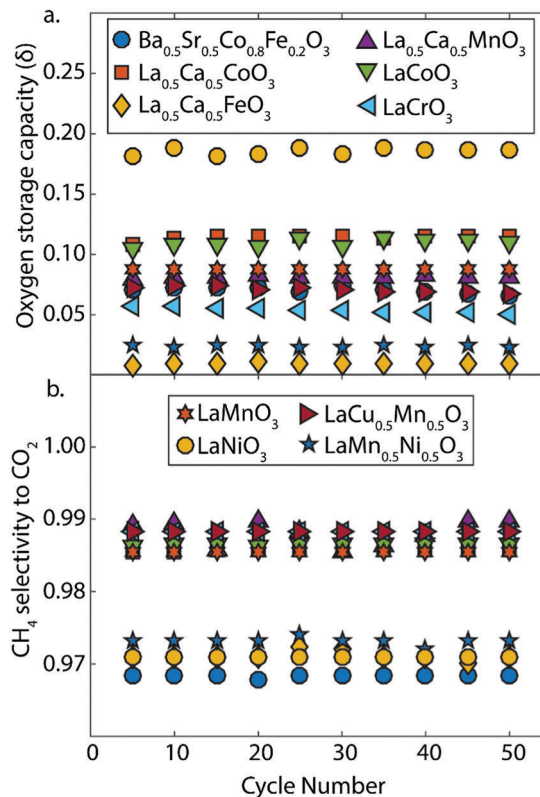
Fig. 1 (a) OSC (δ) and (b) CH_4 selectivity to CO_2 of tested perovskites in 50 cycles with methane at 750 °C in a fixed-bed reactor.

To determine the ability of each of these samples to act as OCs for the combustion of CH_4, approximately 200 mg of sample were loaded into a quartz flow reactor within a tube furnace.[10] CLC reactivity tests were then performed by alternating the gas flow between 11% CH_4/Ar for 2 minutes (combustion) and 20% O_2/Ar for 5 minutes (regeneration) while the sample was held isothermally at 750 °C. Full experimental details are provided in Section S1 of the ESI.† This experiment was designed to prevent the formation of CO, as is often determined by the reduction extent of the metal oxide. Therefore, it is important to note that the OSC reported here is the oxygen available for the combustion of methane, not the total amount of oxygen available for reaction with methane (i.e. partial reduction or methane cracking).

In this study, we found that A cation substitution has a negligible effect on OSC, but there exists an inverted volcano dependence for transferable oxygen during total methane oxidation with the B cation's electronegativity (Pauling scale). The global reaction between perovskite and methane can be represented as,

$$4ABO_3 + \delta CH_4 \rightarrow 4ABO_{3-\delta} + \delta CO_2 + 2\delta H_2O$$

Thus we can define oxygen storage capacity (OSC) in CLC as δ, which was measured by quantitative analysis of CO_2 in the fuel step. Fig. 1(a) shows the OSC (δ) over 50 CLC cycles in the fixed bed reactor and clearly indicates that all perovskites are stable OCs. The amount of CO_2 produced was quantified from the effluent in the fuel step, and carbon coking generated from

methane thermal decomposition, the major side reaction, is measured by the CO_x species in the air step. Shown in Fig. 1(b), we define CO_2 selectivity as:

$$\gamma_{CO_2} = \frac{n_{CO_2}}{n_C + n_{CO_2}}$$

where n_{CO_2} are the number of moles detected in the fuel step and n_C the number of moles detected in the air step. All the perovskites expressed γ_{CO_2} values higher than 95%, indicating their low coking ratio.[11]

In an attempt to provide some microscopic structural context to these results we show in Fig. 2a the relationship between OSC and λ_B (B site electronegativity) on the Pauling Scale.[12] For the mixed B site samples, a simple molar average was used for λ_B. The resulting plot shows an inverted volcano behavior. Since the OSC's of the samples with mixed La and Ca occupancy on the A site showed negligible difference, we concluded that substituting Ca for La on the A site has a negligible effect of the OSC, which agrees with previous publications.[13–17] This also makes sense considering that the B metal is the redox active center of the perovskite. For comparison, we also plotted the average occupancy of the so-called e_g orbital for the transition metal, as determined by

Fig. 2 The relation of OSC (δ) and (a) the λ_B (B site electronegativity) in methane total oxidation and (b) the e_g electron occupancy.

Suntivich et al.,[14] versus OSC. Although true O_h symmetry is not present in all of these materials, the structural distortions are too minor to invert the basic crystal field splitting energies (i.e. make t_{2g}-derived states higher in energy than the e_g-derived ones). Therefore, we use e_g only as a convenient label across various perovskites in searching for broad trends in properties such as catalytic activity or oxygen storage capacity. In cases where two transition metals are present, only the more catalytically active element was considered. Here, the trend appears less obvious than for λ_B, although a volcano-type relationship does seem plausible. Overall, e_g occupancy does not appear to be as useful a descriptor as B-site electronegativity.

Utilizing a materials descriptor such as electronegativity provides a general understanding of OC design with ABO_3 perovskites given that the underlying mechanisms are still unknown. Past studies have found that oxygen transport and mobility in perovskite structures are highly relevant to their other applications, thus considerable attention has been focused on partial substitutions for the A and B sites to find optimal combinations.[18,19] Recently, Imanieh et al. explored the effect of substituted atom size on the reactivity of hydrocarbons with ABO_3 ($CaMnO_3$) perovskites in order to identify the optimal OC for CLC applications.[20] At high reaction temperature ($>800\ °C$) favoring O_2 release, $CaMnO_3$ perovskite with $\sim10\%$ Sr and Fe doped in the A and B sites, respectively, helps improve their oxygen storage capacity (OSC) due to higher crystalline distortion. X. Dai et al. found that compared to Nd, Eu substitution for La on the A site maintains a relatively high catalytic activity and structural stability during redox reactions.[21]

Since Bockris and Otagawa's work in 1980s, descriptors correlating 5-coordinate surface ions' electronic properties of perovskite oxides and their activities towards oxygen electrocatalysis have attracted a lot of interest.[13] It has been reported that the filling of e_g manifold of the octahedral crystal field of the B cations, mainly related to the oxygen binding to the perovskite surface,[13] can be used as an efficient descriptor for reactivity in oxygen evolution reaction (OER) in fuel cell applications employing perovskites[14] and water-splitting reactions.[15] Thus e_g in perovskite, contributed to occupied valence band states, are responsible for the reactive states near Fermi level, could be used as an effective descriptor, consistent with Norskov's d-band theory. From our own results, however, it appears that e_g occupancy is not as relevant for temperature-driven redox reactions.

The role of B-site electronegativity could be related to that of the B–O bond strength. Electronegativity, as defined by Mulliken, is the average of the ionization potential and the electron affinity. Therefore, the degree of hybridization between the B d-states and the O 2p-states would be dependent on electronegativity.

While we have not found a direct correlation between electronegativity and oxide conductivity yet, other workers have found oxygen vacancy formation as a useful descriptor for electrochemical applications of perovskite oxides. Kitchin et al. used density function theory (DFT) calculations to correlate the decrease in the oxygen vacancy formation energy to increasing atomic numbers from Cr to Cu in $LaBO_3$ and $SrBO_3$, which were explored as anode materials in SOFC's.[22] Through DFT calculations,
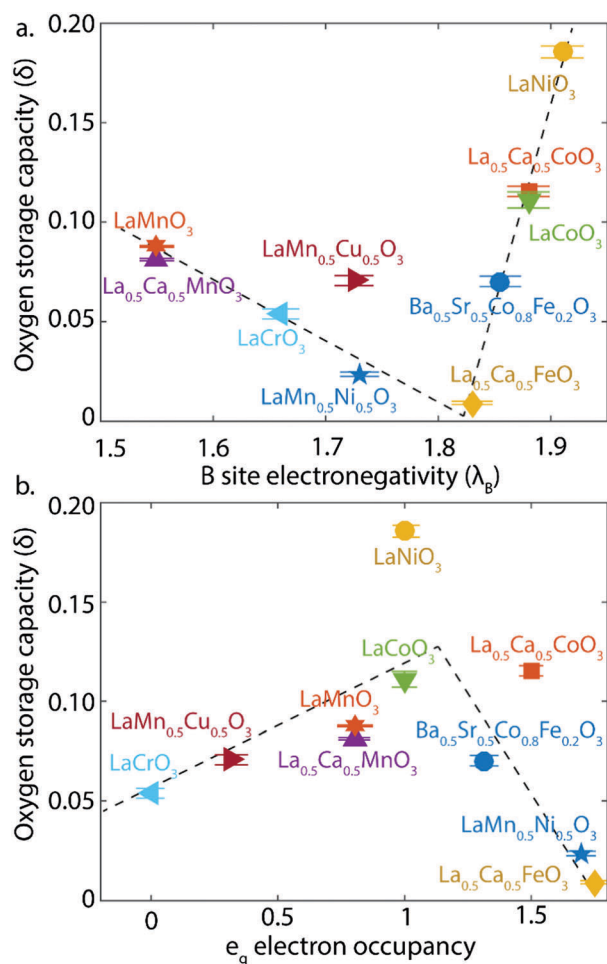
Carter *et al.* demonstrated that ion diffusion in the La$_{1-x}$Sr$_x$BO$_3$ family (B = Cr, Mn, Fe, Co) and Sr$_2$Fe$_{2-x}$Mo$_x$O$_6$ depends on two processes: oxygen vacancy formation and vacancy mediated oxygen migration, and found that oxygen vacancy formation energy could be used as a descriptor for oxide ion transport properties' evaluation.[18]

Yang *et al.* utilized X-ray Absorption Near Edge Structure (XANES) and fluorescence O K-edge to study the effects of the B and A site, respectively, on the electronic structure and found that changes in A site substitution have less of an effect relative to the B-site, and increasing the B site electron count can increase hybridization between the transition metal 3d and oxygen 2p states and therefore covalency.[16] Hong *et al.* reported that partial substitution of the B site could result in improved catalytic effects owing to lattice defects.[23] As to the reaction of perovskites with hydrocarbons, the activation of the C–H bond has been proposed to be important.[19]

For example, the reaction of oxides with methane can follow two pathways, the 4-centered (CH$_3$–B–H–O) transition state (σ-bond metathesis) and 3-centered (CH$_3$–B–H) transition state (dehydrogenation).[11,24] However, our studies are not mechanistic in nature and we cannot propose any of these transition states in our oxides during CLC.

On the left side of the inverted plot (Fig. 2a), the downward trend in the oxygen storage capacity includes B cations with relative low electronegativity. As the B site's electronegativity increases, transition metal–oxygen bond covalency increases due to the decreased difference in electronegativity between the B cation and oxygen anion. Previous computational studies on similar perovskites concluded that oxide vacancy formation is enhanced by weaker B–O bonds in LaBO$_3$ perovskites.[18] Therefore, the less electronegative metals would enhance oxygen vacancy formation under CLC conditions.

Interestingly, as electronegativity increases, the OSC starts to rise again after iron. The previous argument that the B–O bond strength diminishes oxide vacancy formation seems to be less important for this part of the trend. It has been widely accepted that the catalytic performance of metals follows the Sabatier's principle (interactions between the catalyst and interface needs to be "just right")[25] and the d-band model (the existence of correlation between interaction energy and d-band center in transition metal catalysts).[26] Nwosu *et al.* claims that mixed metal ions from 3d transition metal whose average electronegativities are equivalent to those of noble metals should show similar catalytic performance.[27,28] The study of catalysts for hydrocarbon cracking shows that metals with similar electronegativities would therefore lead to similar catalytic effects.[28,29] Therefore, it could be that the d-band center is influenced by the deeper ionization potentials of the B metals (which factors into λ_B) takes over as a more important parameter than B–O bond strength.

Considering the superior catalytic performance of Ba$_{0.5}$Sr$_{0.5}$Co$_{0.8}$Fe$_{0.2}$O$_3$ in OER,[14] we also prepared this perovskite to validate the inverted volcano plot with no lanthanum/calcium

in A site. As indicated in Fig. 2a, the OSC of Ba$_{0.5}$Sr$_{0.5}$Co$_{0.8}$Fe$_{0.2}$O$_3$ fits reasonably well in the inverted volcano plot, indicating that this behavior is more universal and applies to other A site OC perovskites with 3d transition metals on the B site.

Our study concludes that 3d transition metal B site electronegativity could be used as a useful descriptor in choosing perovskite oxygen carriers for combustion of CH$_4$. We found an inverted volcano plot relationship for the lanthanum/calcium perovskite series. While the choice for the A site (either La or Ca) has a negligible effect on the OSC, the choice of the B site is more relevant towards the design of optimal OC's.

Notes and references

1 H. J. Richter and K. F. Knoche, *ACS Symp. Ser.*, 1983, **235**, 71–85.
2 K. Aleklett, M. Höök, K. Jakobsson, M. Lardelli, S. Snowden and B. Söderbergh, *Energy Policy*, 2010, **38**, 1398–1414.
3 A. Lyngfelt, B. Leckner and T. Mattisson, *Chem. Eng. Sci.*, 2001, **56**, 3101–3113.
4 S. Luo, L. Zeng and L. S. Fan, *Annu. Rev. Chem. Biomol. Eng.*, 2015, **6**, 53–75.
5 Z. Sarshar, F. Kleitz and S. Kaliaguine, *Energy Environ. Sci.*, 2011, **4**, 4258.
6 A. Abad, F. García-Labiano, P. Gayán, L. F. de Diego and J. Adánez, *Chem. Eng. J.*, 2015, **269**, 67–81.
7 R. W. Cheary and A. Coelho, *J. Appl. Crystallogr.*, 1992, **25**, 109–121.
8 X. Guo, G. Fang, G. Li, H. Ma, H. Fan, L. Yu, C. Ma, X. Wu, D. Deng, M. Wei, D. Tan, R. Si, S. Zhang, J. Li, L. Sun, Z. Tang, X. Pan and X. Bao, *Science*, 2014, **344**, 616–619.
9 F. X. Li, Z. C. Sun, S. W. Luo and L. S. Fan, *Energy Environ. Sci.*, 2011, **4**, 876–880.
10 L. Liu and M. R. Zachariah, *Energy Fuels*, 2013, **27**, 4977–4983.
11 Y.-H. Chin, C. Buda, M. Neurock and E. Iglesia, *J. Am. Chem. Soc.*, 2011, **133**, 15958–15978.
12 L. Pauling, *Nature of the Chemical bond*, Cornell University Press, 1960.
13 J. O. Bockris and T. Otagawa, *J. Electrochem. Soc.*, 1984, **131**, 290–302.
14 J. Suntivich, K. J. May, H. A. Gasteiger, J. B. Goodenough and Y. Shao-Horn, *Science*, 2011, **334**, 1383–1385.
15 A. Vojvodic and J. K. Norskov, *Science*, 2011, **334**, 1355–1356.
16 W. T. Hong, M. Risch, K. A. Stoerzinger, A. Grimaud, J. Suntivich and Y. Shao-Horn, *Energy Environ. Sci.*, 2015, **8**, 1404–1427.
17 S. Bhavsar and G. Veser, *Energy Fuels*, 2013, **27**, 2073–2084.
18 A. B. Munoz-Garcia, A. M. Ritzmann, M. Pavone, J. A. Keith and E. A. Carter, *Acc. Chem. Res.*, 2014, **47**, 3340–3348.
19 H. Zhu, P. Zhang and S. Dai, *ACS Catal.*, 2015, **5**, 6370–6385.
20 M. H. Imanieh, M. H. Rad, A. Nadarajah, J. González-Platas, F. Rivera-López and I. R. Martín, *J. CO$_2$ Util.*, 2016, **13**, 95–104.
21 X. P. Dai, R. J. Li, C. C. Yu and Z. P. Hao, *J. Phys. Chem. B*, 2006, **110**, 22525–22531.
22 M. T. Curnan and J. R. Kitchin, *J. Phys. Chem. C*, 2014, **118**, 28776–28790.
23 S. Carter, A. Selcuk, R. J. Chater, J. Kajda, J. A. Kilner and B. C. H. Steele, *Solid State Ionics*, 1992, **53**, 597–605.
24 S. Ponce, M. A. Peña and J. L. G. Fierro, *Appl. Catal., B*, 2000, **24**, 193–205.
25 O. Deutschmann, H. Knözinger, K. Kochloefl and T. Turekin, Heterogeneous Catalysis and Solid Catalysts, *Ullmann's Encyclopedia of Industrial Chemistry*, Electronic Release, Willey-VCH Verlag, Weinheim, 7th edn, 2009.
26 J. K. Norskov, T. Bligaard, J. Rossmeisl and C. H. Christensen, *Nat. Chem.*, 2009, **1**, 37–46.
27 C. Nwosu, *J. Tech. Sci. Tech.*, 2012, **1**, 25–28.
28 M. A. Plummer, *US Pat.*, 4557803, 1985.
29 B. Al Alwan, S. O. Salley and K. Y. S. Ng, *Appl. Catal., A*, 2014, **485**, 58–66.